Integrin α5β1 regulates PP2A complex assembly through PDE4D in atherosclerosis

Sanguk Yun,[1] Rui Hu,[1] Melanie E. Schwaemmle,[1] Alexander N. Scherer,[2] Zhenwu Zhuang,[1] Anthony J. Koleske,[2] David C. Pallas,[3] and Martin A. Schwartz[1,4,5]

[1]Department of Internal Medicine, Yale Cardiovascular Research Center, and [2]Department of Molecular Biophysics and Biochemistry, Yale University, New Haven, Connecticut, USA. [3]Department of Biochemistry, Emory University School of Medicine, Atlanta, Georgia, USA. [4]Department of Biomedical Engineering, and [5]Department of Cell Biology, Yale University, New Haven, Connecticut, USA.

Fibronectin in the vascular wall promotes inflammatory activation of the endothelium during vascular remodeling and atherosclerosis. These effects are mediated in part by fibronectin binding to integrin α5, which recruits and activates phosphodiesterase 4D5 (PDE4D5) by inducing its dephosphorylation on an inhibitory site, S651. Active PDE then hydrolyzes antiinflammatory cAMP to facilitate inflammatory signaling. To test this model in vivo, we mutated the integrin binding site of PDE4D5 in mice. This mutation reduced endothelial inflammatory activation in atherosclerosis-prone regions of arteries and, in a hyperlipidemia model, reduced atherosclerotic plaque size while increasing markers of plaque stability. We then investigated the mechanism of PDE4D5 activation. Proteomics identified the PP2A regulatory subunit B55α as the factor recruiting PP2A to PDE4D5. The B55α-PP2A complex localized to adhesions and directly dephosphorylated PDE4D5. This interaction also, unexpectedly, stabilized the PP2A-B55α complex. The integrin-regulated, proatherosclerotic transcription factor Yap was also dephosphorylated and activated through this pathway. PDE4D5 therefore mediated matrix-specific regulation of endothelial cell phenotype via an unconventional adapter role, assembling and anchoring a multifunctional PP2A complex that has other targets. We believe these results may have widespread consequences for the control of cell function by integrins.

Introduction

Endothelial basement membranes in stable vessels, consisting primarily of collagen IV, laminins, and less abundant species, promote vessel maturation and stability (1, 2). By contrast, fibronectin (FN) is present at low levels in stable vessels in most tissues but is strongly upregulated in inflammation, developmental and postnatal angiogenesis, and atherosclerosis, as is its main receptor integrin α5β1 (3–6). FN has been most studied in atherogenesis, where it contributes to plaque formation (7). These effects are mediated in part by inhibition of the antiinflammatory cAMP/protein kinase A (cAMP/PKA) pathway (8). This occurs through binding of the α5 subunit cytoplasmic domain to the cAMP-specific phosphodiesterase PDE4D5, which results in dephosphorylation of PDE4D5 on an inhibitory site (9). The resultant increase in PDE catalytic activity suppresses cAMP/PKA signaling, thus priming endothelial cells (ECs) for inflammatory activation.

EC responses to fluid shear stress play major roles in vessel function, remodeling, and disease. Shear stress regulates artery remodeling to determine lumen diameter and during angiogenesis stabilizes vessel sprouts once flow is reestablished (10, 11). Disturbed flow patterns that arise in regions of arteries that curve sharply or branch induce local EC inflammatory activation. In the presence of systemic risk factors such as hyperlipidemia, hyperglycemia, hypertension, and elevated inflammatory mediators, these regions selectively develop atherosclerotic plaques. FN gene expression and matrix assembly are induced by disturbed flow (12, 13). FN is deposited at atherosclerosis-prone regions of arteries in WT mice and increases in atherosclerotic lesions in mice and humans (4, 14). Deletion of each of the individual isoforms of FN reduces plaque size in mice (15–17). However, in the 1 study in which it was examined, deletion of plasma FN also resulted in thinner fibrous caps with evidence of plaque rupture, suggesting reduced plaque stability (17).

Adherence of cells to FN promoted activation of NF-κB and other inflammatory pathways in response to disturbed flow, IL-1β, and oxidized LDL compared with adherence to collagens or laminin (4, 9, 18, 19). These effects were reversed by mutation of the integrin α5 cytoplasmic domain in vitro. To test in vivo, we introduced this mutation into mice, which suppressed atherosclerosis and improved recovery from hindlimb ischemia (9, 20). EC-specific deletion of integrin α5 also strongly reduced atherosclerosis in mouse models (21). However, other integrin α5 cytoplasmic domain effectors may also mediate these effects (22).

We set out to rigorously test the extent to which binding of PDE4D5 to integrin α5 mediates the role of α5 in vascular inflammation and atherosclerosis. Because complete deletion of PDE4D results in neonatal growth retardation and lethality (23), we mutated the integrin binding sequence in PDE4D5 to block this interaction without interfering with other functions. Positive results then prompted us to further examine the mechanism of PDE4D5 regulation. These studies revealed that PDE4D5 regulates a wider array of pathways via effects on phosphatase PP2A and other downstream targets.

Conflict of interest: The authors have declared that no conflict of interest exists.

Submitted: January 25, 2019; **Accepted:** August 7, 2019; **Published:** October 7, 2019.
Reference information: *J Clin Invest*. 2019;129(11):4863–4874.
https://doi.org/10.1172/JCI127692.

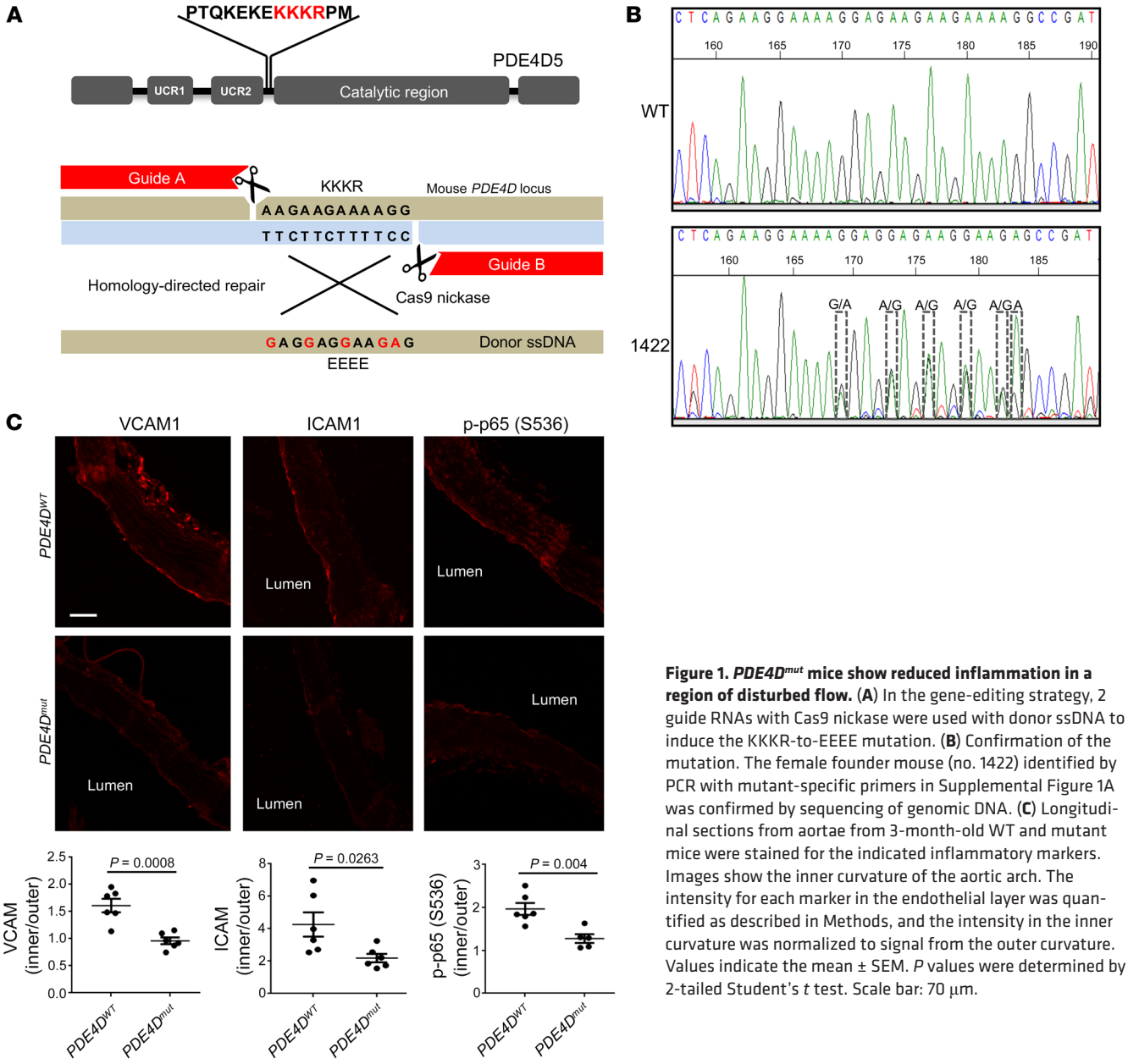

Figure 1. *PDE4D*^{mut} mice show reduced inflammation in a region of disturbed flow. (**A**) In the gene-editing strategy, 2 guide RNAs with Cas9 nickase were used with donor ssDNA to induce the KKKR-to-EEEE mutation. (**B**) Confirmation of the mutation. The female founder mouse (no. 1422) identified by PCR with mutant-specific primers in Supplemental Figure 1A was confirmed by sequencing of genomic DNA. (**C**) Longitudinal sections from aortae from 3-month-old WT and mutant mice were stained for the indicated inflammatory markers. Images show the inner curvature of the aortic arch. The intensity for each marker in the endothelial layer was quantified as described in Methods, and the intensity in the inner curvature was normalized to signal from the outer curvature. Values indicate the mean ± SEM. *P* values were determined by 2-tailed Student's *t* test. Scale bar: 70 μm.

Results

PDE4D^{mut} *mice*. We previously mapped the integrin α5 binding site in PDE4D5 to a short basic sequence (KKKR) in the linker region between the N-terminal UCR2 domain and the catalytic domain (9). Replacement of this sequence with EEEE abolished binding to integrin α5 and blocked the proinflammatory effect of FN in vitro. In this study, we aimed to probe its function in vivo by engineering this mutation into mice using CRISPR/Cas9 technology (Figure 1A). To minimize off-target mutations, we used the double-nicking strategy with Cas9 nickase and 2 guide RNAs that recognize flanking target sequences (24) (Figure 1A). From 15 pups, sequencing and genotyping identified 1 mouse with the correct mutation (Figure 1B and Supplemental Figure 1A; 1 female founder, 3 indel mutants, and 11 WT mice; supplemental material available online with this article; https://doi.org/10.1172/JCI127692DS1). The mutated allele was successfully transmitted to the next generation (Supplemental Figure 1B). Homozygous mice were born at the expected Mendelian ratio (WT: 28, heterozygous: 45, homozygous: 20) and were viable and fertile, without obvious abnormalities. PDE4D expression was similar in the *PDE4D*^{mut} mice compared with that in WT mice (Supplemental Figure 1C).

ECs in atherosclerosis-prone regions of arteries in WT mice showed elevated inflammatory markers that coincide with FN accumulation (4, 9). To investigate the effects of the PDE4D5 mutation, longitudinal sections of aortae from 3-month-old mice were examined for inflammatory markers in the endothelium in the inner curvature of the aortic arch, a well-characterized region of disturbed flow that is prone to atherosclerosis when hyperlipidemia and other risk factors are present. As expected, ICAM1, VCAM1, and phosphorylated NF-κB p65 (p–NF-κB p65) were all elevated in this region in WT mice (quantified as the ratio of staining relative to the atherosclerosis-resistant outer curvature in each

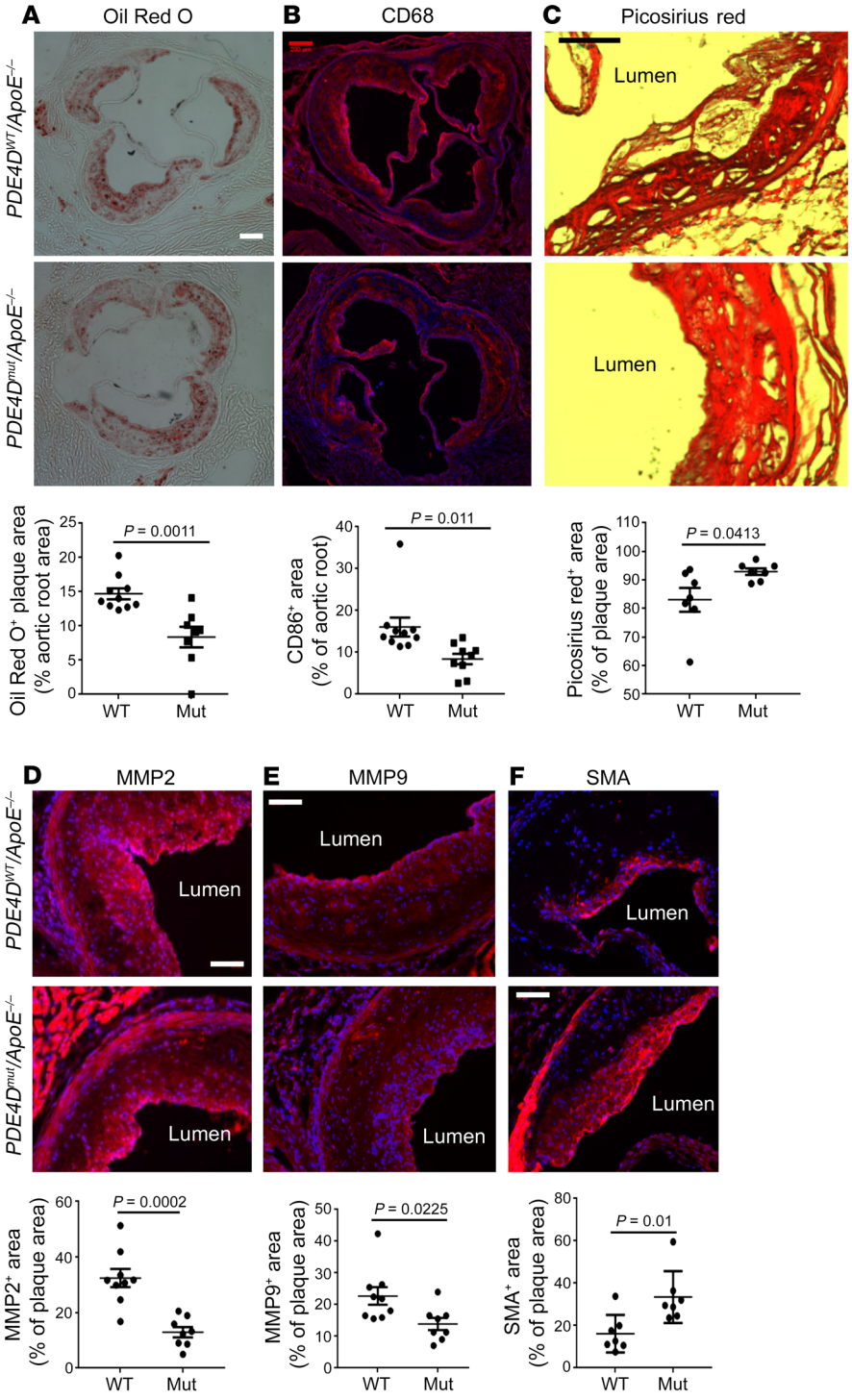

Figure 2. Atherosclerosis and recovery from hindlimb ischemia. (**A**) Aortic root sections from WT and *PDE4D*^{mut} *ApoE*$^{-/-}$ mice after 4 months on a high-fat diet were stained with Oil Red O to determine lesion size. (**B**) Sections were stained for CD68 to identify macrophages. (**C**–**E**) To analyze plaque composition, sections were stained for fibrillar collagens with Picrosirius red (**C**), MMP2 (**D**), and MMP9 (**E**). (**F**) Sections were stained for SMA to identify smooth muscle cells. In all cases, the staining intensity was quantified as described in Methods and normalized to total plaque area. Scale bars: 200 μm (**A** and **B**) and 100 μm (**C**–**F**). *P* values were determined by Student's *t* test. Mut, mutant.

mouse); these markers were all significantly (ICAM1) or completely (NF-κB and VCAM1) suppressed in *PDE4D*^{mut} mice (Figure 1C). Preventing the binding of PDE4D5 to integrin α5 thus inhibits vascular inflammation in a manner similar to that seen with mutation of the α5 cytoplasmic domain (25).

Next, *PDE4D*^{mut} mice were bred onto an ApoE-null background and fed a high-fat Western diet for 4 months to induce atherosclerotic lesions. The PDE mutation had no effect on serum lipids (Supplemental Figure 2A). Oil Red O staining of aortic roots showed that atherosclerotic lesions were significantly reduced in *PDE4D*^{mut} *ApoE*-null (*PDE4D*^{mut} *ApoE*$^{-/-}$) mice compared with WT *ApoE*$^{-/-}$ mice (*PDE4D*^{WT} *ApoE*$^{-/-}$) (Figure 2A). CD68 staining for macrophages was similarly reduced (Figure 2B). Previous studies showed evidence of plaque vulnerability after deletion of plasma FN (26). However, smooth muscle actin (SMA), quantified per plaque area, was increased by 50% in *PDE4D*^{mut} mice (Figure 2F); Picrosirius red staining for fibrillar collagen was also higher in *PDE4D*^{mut} mice (Figure 2C). By contrast, staining for MMP2 and MMP9 per area of plaque was reduced (Figure 2, D and E), as was MMP activity (Supplemental Figure 2C). *ApoE*$^{-/-}$ mice on a high-

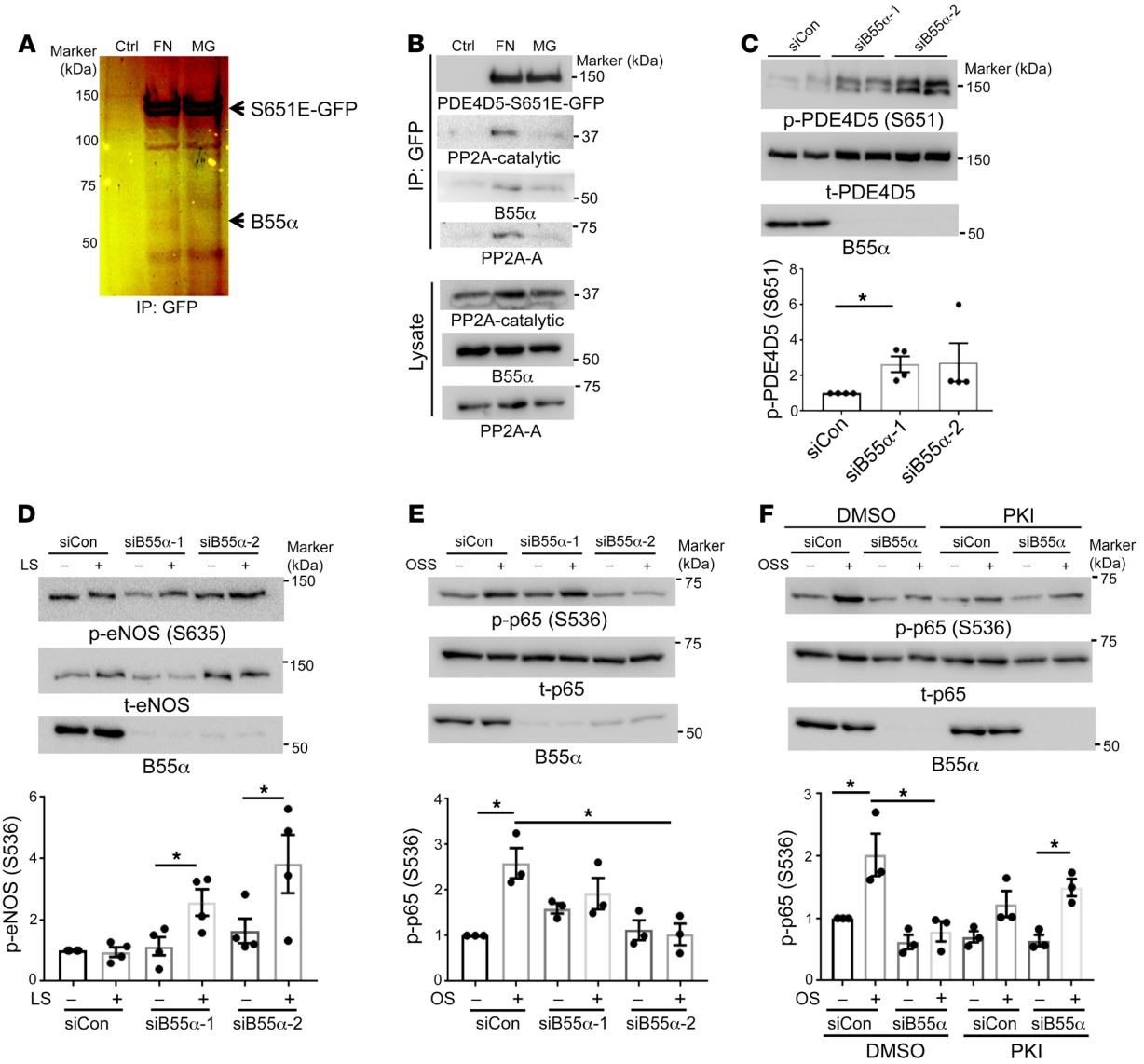

Figure 3. B55α is required for PP2A-dependent PDE4D dephosphorylation. (**A**) FN promoted B55α binding to PDE4D5. BAECs stably expressing GFP-tagged PDE4D5-S651E were plated on dishes coated with FN or MG for 20 minutes. Lysates were immunoprecipitated with GFP-Trap. SDS-PAGE and silver staining identified a FN-specific band at approximately 55 kDa, which was identified by LC-MS (see Supplemental Figure 3) as B55α. (**B**) Confirmation of proteomic results. PDE4D5-S651E immune complexes prepared as in **A** were subjected to Western blotting to detect PP2A subunits as indicated. Results are representative of 3 independent experiments. (**C**) For B55α knockdown, BAECs expressing WT GFP-tagged PDE4D5 were transfected with control or B55α siRNAs and plated on FN for 6 hours. Cell lysates were Western blotted for p-PDE4D (S651) or total PDE4D (t-PDE5D) ($n = 4$). (**D**) BAECs transfected with control siRNA (siCon) or B55α siRNA were plated on FN and exposed to laminar shear (LS) for 15 minutes. Flow-dependent S635 phosphorylation of eNOS was measured by immunoblotting with a phosphorylation-specific Ab ($n = 4$). (**E**) BAECs transfected with control or B55α siRNAs were plated on FN and subjected to OSS for 2 hours. NF-κB activation was measured by Western blotting for p-p65 (S536) ($n = 3$). (**F**) BAECs transfected with control or B55α siRNA were plated on FN, treated or not with the PKI 14-22 amide inhibitor (PKI) or DMSO, and subjected to OSS for 2 hours. NF-κB activation was measured by probing for p-p65 (S536) ($n = 3$). *$P < 0.05$, by Kruskal-Wallis test with Dunn's multiple comparisons post hoc test (**C**), 2-tailed Student's *t* test (**D**), or 1-way ANOVA (**E** and **F**). Ctrl, control.

fat diet also showed decreased VCAM1 staining in the inner curvature of the aortic arch (Supplemental Figure 2B). Together, these data show that mutation of the integrin binding site in PDE4D5 reduced atherosclerotic lesion size and inflammatory status in hyperlipidemic mice and increased markers of plaque stability. These results provide definitive evidence that PDE4D5 is a critical integrin α5 effector in this pathway.

Recovery from restriction of arterial flow occurs via both flow-dependent arteriogenesis and ischemia- and VEGF-induced angiogenesis (27, 28). As FN has been implicated in both processes (5, 6, 28, 29), we tested *PDE4D*^{mut} mice using the hindlimb ischemia model, in which ligation of the femoral artery induces ischemia-independent, flow-dependent arteriogenesis in the upper leg and ischemia-induced angiogenesis in the lower leg (30). Three-month-old WT and *PDE4D*^{mut} mice were subjected to femoral artery ligation, and blood flow recovery was monitored by laser Doppler imaging. Blood flow recovery was modestly but significantly enhanced in *PDE4D*^{mut} mice 7 days after ligation

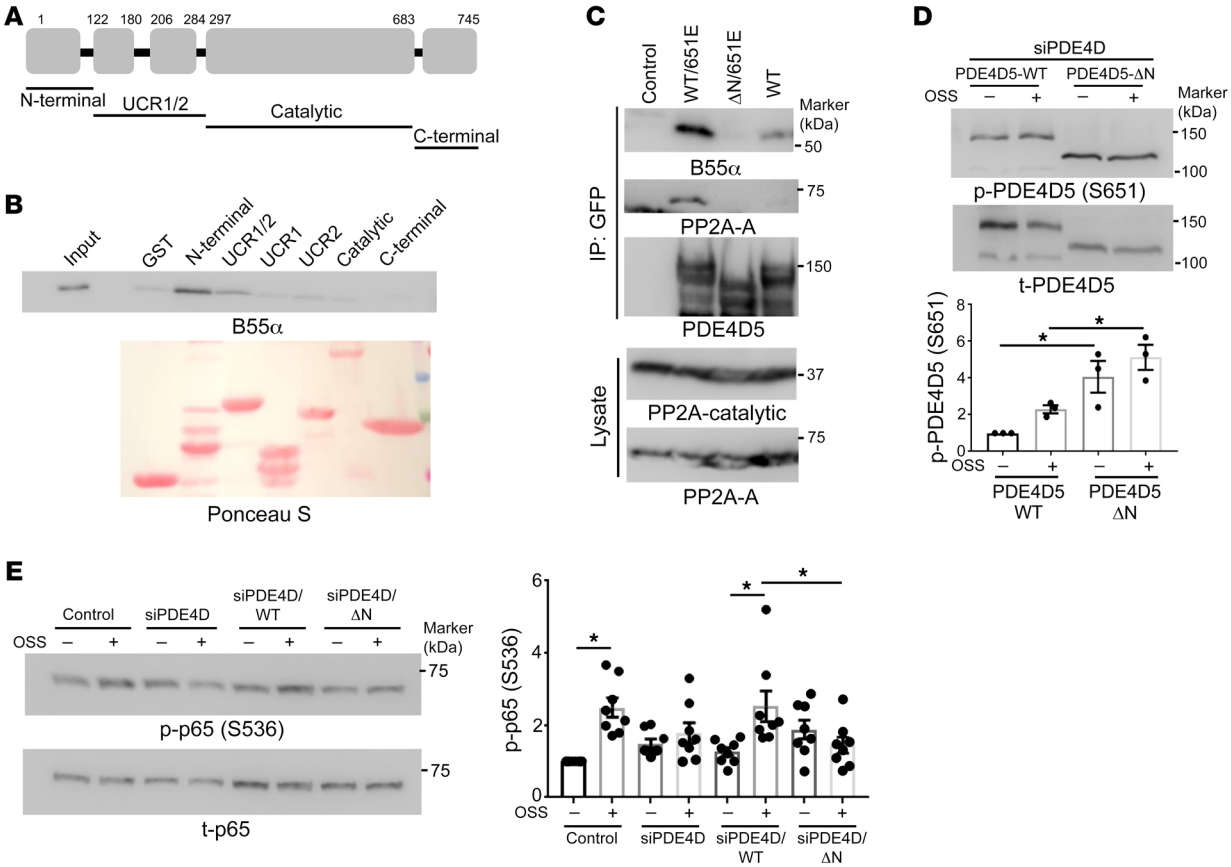

Figure 4. Mapping the B55α binding site on PDE4D5. (**A**) Schematic representation of PDE4D5 fragments. (**B**) Immobilized GST-tagged fragments of PDE4D5 were incubated with purified B55α and then washed and probed for bound B55α ($n = 3$). (**C**) HEK 293T cells were transfected with the indicated GFP-tagged PDE4D constructs. Lysates were immunoprecipitated with GFP-Trap and immune complexes probed for B55α and the PP2A-A subunit ($n = 3$). (**D**) PDE4D5-knockdown BAECs were rescued with WT or the N-terminally deleted mutant (ΔN). Cells were replated on FN and subjected to OSS for 2 hours. PDE4D5 (S651) phosphorylation was assayed as in Figure 3 ($n = 3$). (**E**) The same lysates were probed for p-p65 to assay NF-κB activity ($n = 8$). *$P < 0.05$, by 2-way ANOVA.

(Supplemental Figure 2, D and G). Micro-CT (μCT) showed that *PDE4D*^{mut} mice had higher densities of both large and small vessels in the ischemic legs 14 days after surgery (Supplemental Figure 2, E and F). We observed no differences in vessel density in the control legs (Supplemental Figure 2, H and I), indicating that these effects occurred only after surgery. Specifically blocking the PDE4D5-integrin interaction therefore did not limit, but instead slightly accelerated, vessel remodeling in C57Bl6 mice.

Identification of the PP2A complex that dephosphorylates PDE4D. As PDE4D5 activation appeared to be critical for these effects, we next investigated the mechanism of its activation in more detail. Integrin α5β1 activates PDE4D5 by triggering its dephosphorylation on inhibitory S651 by PP2A, which suppresses antiinflammatory cAMP/PKA signaling (9). PP2A, however, represents a family of enzyme complexes composed of a catalytic subunit (C), scaffolding subunit (A), and regulatory/targeting subunit (B). There are 2 C isoforms, 2 A isoforms, and at least 23 regulatory B subunits that mediate selective substrate binding, subcellular localization, and catalytic activity of PP2A holoenzymes (31). PP2A AC-core dimers dynamically associate with B subunits regulated by posttranslational modification such as phosphorylation and methylation of the C subunit or by adaptor protein binding (32, 33).

To identify the specific PP2A complex mediating FN-dependent PDE4D dephosphorylation, we hypothesized that a phosphomimetic mutant (PDE4D5-S651E) would behave as a phosphatase trapping mutant for affinity chromatography. Cells were therefore transfected with GFP–PDE4D5-S651E, detached from the culture dishes, and replated on dishes coated with FN or laminin/coll IV basement membrane protein (Matrigel [MG]). Lysates were pulled down with GFP-Trap nanobody beads and analyzed by SDS-PAGE and silver staining. We observed a PDE4D5-dependent band at 55 kDa from cells on FN but not MG (Figure 3A). Liquid chromatography/mass spectrometry (LC-MS) proteomics identified the protein as the PP2A-B55α subunit (Supplemental Figure 3). This finding was confirmed by immunoblotting (Figure 3B). Thus, B55α appears to be a FN-specific PP2A regulatory/targeting subunit that binds PDE4D5.

To test its function in this pathway, we knocked down B55α in ECs using 2 different siRNAs. We found that B55α depletion strongly increased PDE4D5 (S651) phosphorylation, supporting its role in PDE4D5 dephosphorylation (Figure 3C). To test the role of cAMP and PKA, we examined the specific PKA site (S635) on eNOS (34). B55α was knocked down in ECs, which were plated on FN and stimulated by flow. Phosphorylation of eNOS

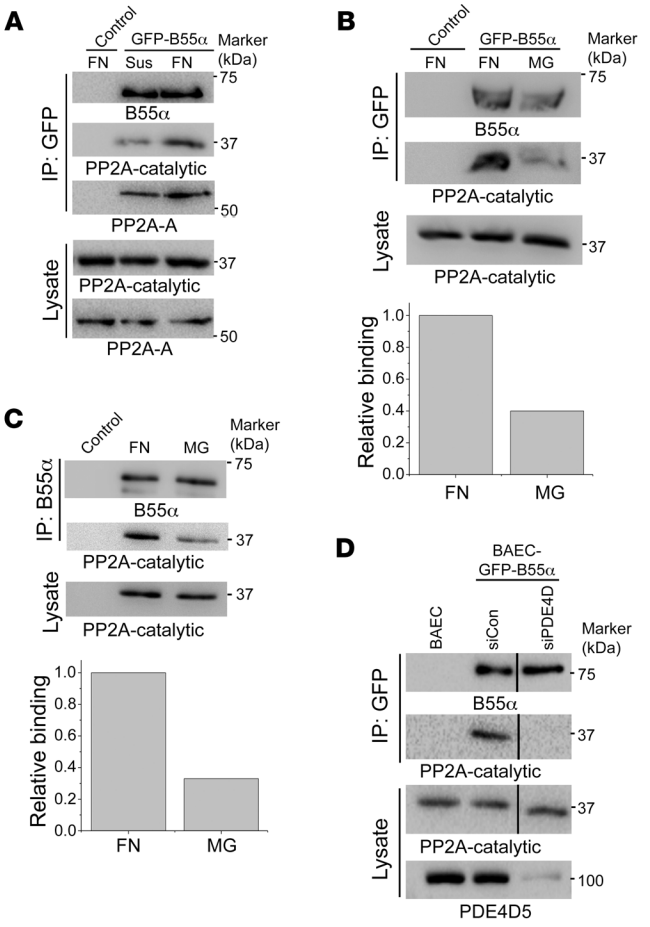

Figure 5. ECM-dependent PP2A-B55α assembly. (**A**) BAECs expressing GFP-B55α were detached and replated on FN or kept in suspension (Sus) for 20 minutes. GFP-B55α was immunoprecipitated, and PP2A subunits were probed in the immune complexes. (**B**) BAECs expressing GFP-B55α were replated on FN or MG. GFP-B55α binding with B subunits was assayed as in **A** (n = 3). (**C**) BAECs were replated on FN or MG. Endogenous B55α was immunoprecipitated and the catalytic subunit assessed by Western blotting. (**D**) BAECs transfected with PDE4D siRNA were replated on FN for 20 minutes. GFP-B55α was immunoprecipitated and the catalytic subunit assayed by Western blotting as in **A** (n = 3).

(S635) [p-eNOS (S635)] is normally suppressed by FN (19) but was increased following B55α depletion (Figure 3D). Consistent with high cAMP/PKA signaling, NF-κB activation by oscillatory shear stress (OSS) was also inhibited (Figure 3E). To test whether the reduced NF-κB activation was mediated by PKA, cells were treated with the specific PKA inhibitor myristoylated PKI (14-22) amide. This treatment restored flow-dependent NF-κB activation after B55α depletion (Figure 3F). Together, these results show that B55α is required for dephosphorylation and activation of PDE4D5, which reduces cAMP/PKA signaling to promote NF-κB activation in cells on FN.

B55α directly binds the N-terminal domain of PDE4D5. The identification of B55α as the regulatory/targeting subunit that mediates the association of the PP2A complex with PDE4D5 at sites of adhesion raised the question of whether this interaction is direct. We therefore measured binding of purified recombinant B55α to purified recombinant fragments of PDE4D5 (Figure 4A). B55α specifically bound to the N-terminal domain (amino acids 1–122) of PDE4D5 (Figure 4B). Deleting this region from the S651E mutant of PDE4D5 (which bound PP2A more efficiently than did WT; Figure 4C) abolished the interaction with B55α (Figure 4C). Thus, the N-terminal domain of PDE4D5 mediates direct binding.

To test the functional role of this interaction, we asked whether the N-terminal domain is required for PDE4D5 (S651) dephosphorylation. Thus, endogenous PDE4D5 was knocked down and cells rescued with WT or the ΔN mutant. p-PDE4D5 (S651) was increased with the ΔN mutant relative to WT protein in cells on FN (Figure 4D). To test the role of this interaction in inflammatory activation by disturbed flow, we carried out a similar knockdown-rescue protocol and then exposed the cells to oscillatory flow for 2 hours. As expected, NF-κB activation by disturbed flow was blocked by PDE4D5 depletion and rescued by WT PDE4D5 but not the ΔN mutant (Figure 4E). Together, these data show that direct binding of PDE4D to B55α promotes PDE4D5 dephosphorylation, which facilitates EC inflammatory activation by disturbed flow.

FN promotes PP2A-B55α holoenzyme assembly. During these analyses, we unexpectedly observed that plating cells on FN greatly increased the co-IP between GFP-B55α and the catalytic subunit of PP2A compared with nonadherent cells (Figure 5A) or cells on MG (Figure 5B). To confirm these results, we immunoprecipitated endogenous B55α, which also showed increased association with the catalytic subunit when plated on FN relative to MG (Figure 5C). To test whether this effect requires PDE4D, we performed similar co-IP experiments after knockdown of PDE4D. We found that PDE4D depletion blocked assembly of the PP2A complex in cells on FN (Figure 5D). Thus, FN promotes the assembly of a PP2A phosphatase complex, which requires PDE4D5. To our knowledge, this is the first instance in which a receptor interaction controls the assembly of a phosphatase complex.

These results suggest that B55α may localize to cell-matrix adhesions through its association with PDE4D5. To test this idea, cells expressing GFP-B55α were plated on FN or MG and examined with and without application of shear stress. Shear stress induced B55α relocalization to adhesions that partially overlapped paxillin (Supplemental Figure 4, A and B). Given the round shape of the adhesions, we examined whether those adhesions were spreading initiation centers (SICs) that formed transiently during cell spreading (35). RACK1, a SIC marker, showed flow-dependent colocalization with B55α on FN (Supplemental Figure 4C). Shear stress–induced B55α localization to sites of adhesion occurred preferentially on FN compared with MG (Supplemental Figure 4A). These results suggest that binding of cells to FN promotes PP2A holoenzyme assembly at sites of adhesion through an integrin/PDE4D5/B55α pathway.

Yap dephosphorylation by PP2A-B55α. Cells contain tens of thousands of phosphorylated residues and many fewer phosphatase complexes; our finding that FN and integrin α5 control the assembly of a major phosphatase complex therefore immediately suggested that there may be other functionally relevant substrates. The transcriptional regulator Yap is linked to integrin signaling, endothelial inflammation, and atherosclerosis (36, 37). In ECs, disturbed flow induces Yap dephosphorylation, stabilization, nuclear

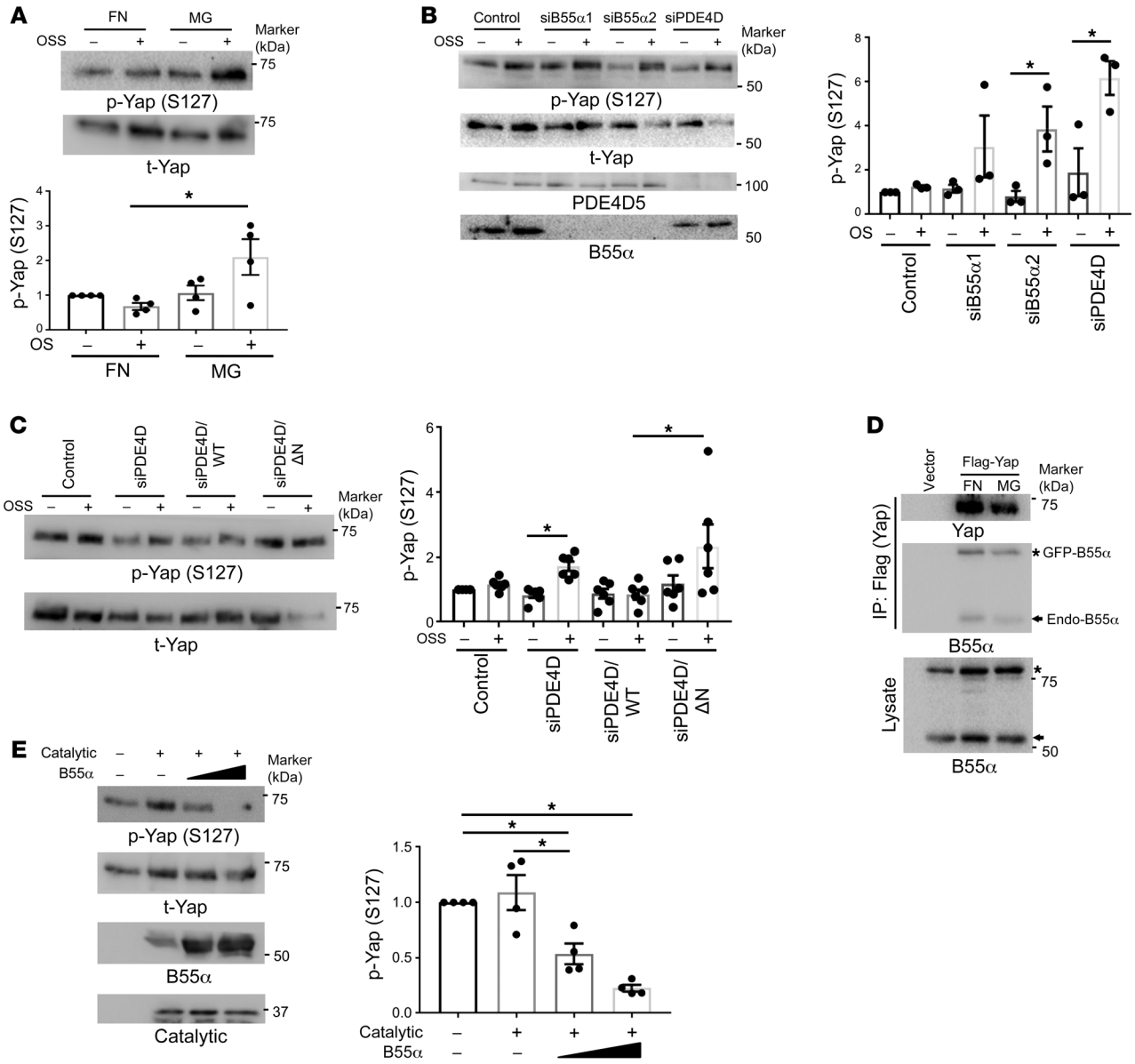

Figure 6. Yap is a PP2A-B55α substrate. (**A**) BAECs plated on FN or MG for 6 hours were exposed to OSS for 2 hours. Phosphorylation of Yap (S127) was assayed by Western blotting ($n = 4$). (**B**) HUVECs transfected with B55α siRNA or PDE4D siRNA were detached and replated on FN and then sheared for 2 hours. Lysates were analyzed by Western blotting for p-Yap (S127). $n = 3$ independent experiments. (**C**) PDE4D5-knockdown BAECs were reconstituted with WT or N-terminally deleted mutant (ΔN). Cells were replated on FN, subjected to OSS for 2 hours, and Yap S127 phosphorylation assayed as in **A** ($n = 6$). (**D**) BAECs expressing GFP-B55α were transfected with Flag-Yap and replated on FN or MG for 20 minutes. Yap was immunoprecipitated with Flag Ab and probed for B55α. $n = 3$ independent experiments. (**E**) In the in vitro phosphatase assay, the PP2A catalytic subunit was immunoprecipitated with the PP2A C subunit Ab (clone 1D6) and incubated for 30 minutes at 37°C with p-Yap in the presence of increasing amounts of purified B55α. Reaction mixtures were immunoblotted for p-Yap (S127) ($n = 4$). $^*P < 0.05$, by 1-way ANOVA (**A** and **E**) and 2-tailed Student's t test (**B** and **C**).

translocation, and transcription of target genes including inflammatory mediators (36, 37). Yap phosphorylation by the upstream kinases LATS1 and LATS2 inhibits Yap function via phosphorylation of S127, which results in Yap retention in the cytoplasm (38), and S381, which triggers Yap degradation (39). Yap may be dephosphorylated by PP2A in virus-transformed cells (40). However, the phosphatases that reverse these events under normal circumstances are poorly defined. We therefore examined Yap in our system.

To test whether Yap phosphorylation is matrix dependent, we plated ECs on FN or MG. We observed that adherence to FN, but not MG, triggered rapid Yap S127 dephosphorylation (Supplemental Figure 5A). Disturbed flow induced Yap phosphorylation in cells on MG, which was completely suppressed on FN (Figure 6A). These results indicate that a collagen/laminin basement membrane represses Yap activation, consistent with vascular stabilization, whereas FN promotes Yap activation, consistent with its proinflammatory effects.

To test whether these matrix-specific effects involved the PP2A complex, cells were transfected with B55α siRNA. Yap dephosphorylation in cells on FN was prevented by knock-down of

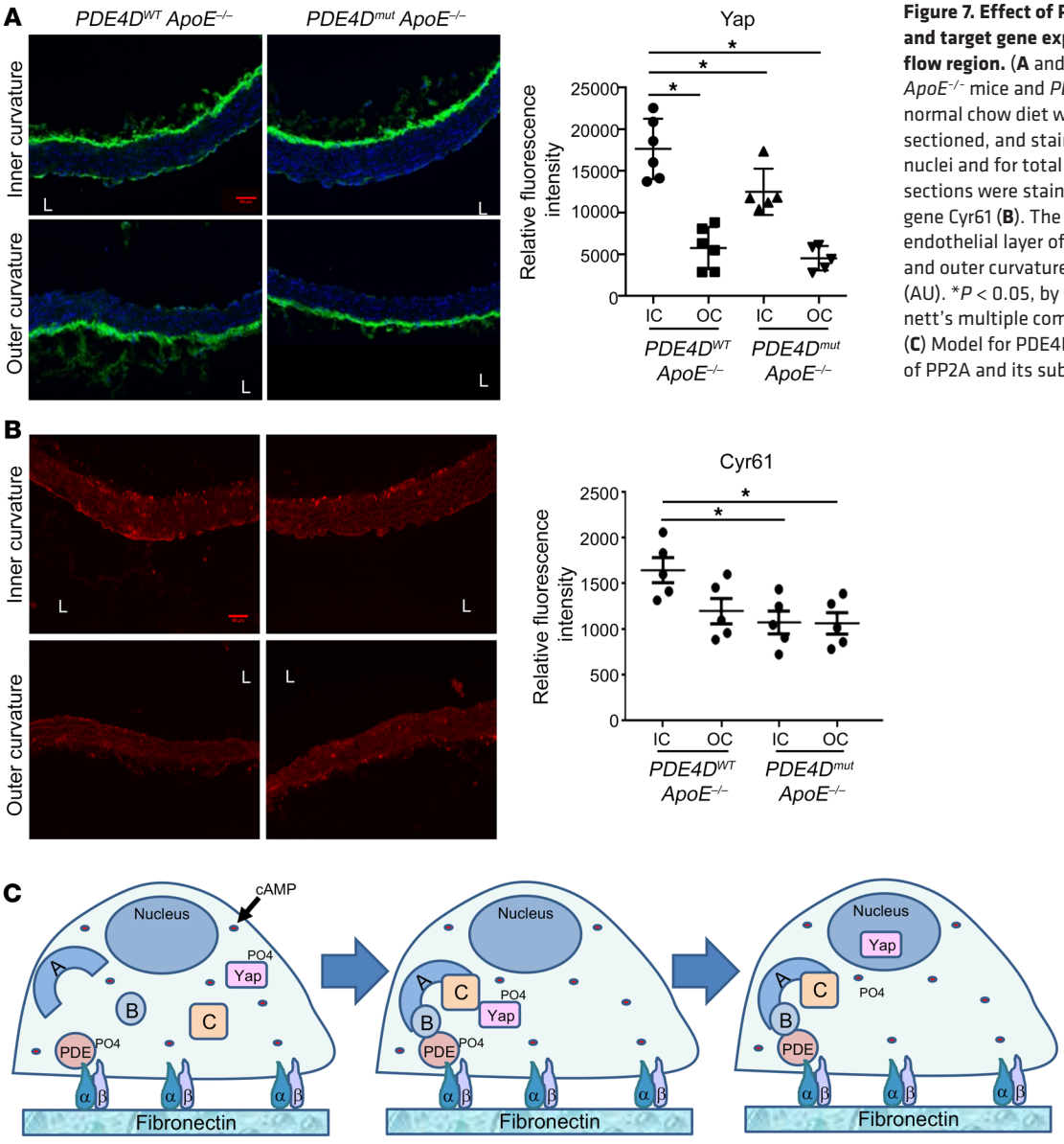

Figure 7. Effect of PDE4D mutation on Yap and target gene expression in a disturbed flow region. (**A** and **B**) Aortae from *PDE4D*^{WT} *ApoE*$^{-/-}$ mice and *PDE4D*^{mut} *ApoE* mice on a normal chow diet were fixed, longitudinally sectioned, and stained for DAPI to identify nuclei and for total Yap (**A**). The adjacent sections were stained for the Yap target gene Cyr61 (**B**). The mean intensity in the endothelial layer of the inner curvature (IC) and outer curvature (OC) was quantified (AU). *$P < 0.05$, by 1-way ANOVA with Dunnett's multiple comparisons test (**A** and **B**). (**C**) Model for PDE4D-dependent regulation of PP2A and its substrate Yap. L, lumen.

B55α (Figure 6B and Supplemental Figure 5, B and C). Yap dephosphorylation was also blocked by knockdown of PDE4D (Figure 6B and Supplemental Figure 5C), which was rescued by WT but not the B55α-binding–deficient PDE4D-ΔN mutant (Figure 6C). Yap nuclear translocation also increased on FN (Supplemental Figure 5D), which was blocked by knockdown of B55α or PDE4D (Supplemental Figure 5E). Yap S127 dephosphorylation correlated with induction of the Yap target genes ANKRD1 and Cyr61, which was also blocked by B55α or PDE4D knockdown (Supplemental Figure 5F). Consistent with reduced Yap (S381) dephosphorylation, the previously reported increase in Yap protein levels under longer-term disturbed flow (36) was abolished by knockdown of B55α or PDE4D (Supplemental Figure 5G). Together, these results show that the integrin/PDE4D5/B55α axis controls Yap activity.

To identify the direct PP2A-B55α target in the Hippo/Yap pathway, we first examined the upstream kinase LATS1. In cells on FN, flow decreased LATS1 phosphorylation, however, this was unaffected by B55α knockdown (Supplemental Figure 6). This result excludes LATS1 and all upstream steps in the pathway. We therefore examined Yap itself. Immunoprecipitated Flag-Yap associated with both GFP-B55α and endogenous B55α (Figure 6D). To test whether Yap is a direct PP2A substrate, we measured Yap dephosphorylation in vitro with purified components. Highly phosphorylated Yap purified from confluent HEK 293T cells was incubated with the PP2A catalytic subunit immunoprecipitated from ECs using an Ab (clone 1D6) that specifically recognizes the catalytic subunit without the bound B subunit (41). The catalytic subunit alone showed negligible activity toward p-Yap, however, addition of purified B55α induced dose-dependent Yap (S127) dephosphorylation (Figure 6E). Thus, p-Yap is a direct, B55α-dependent PP2A target.

These results predicted that the previously reported activation and stabilization of Yap in regions of disturbed flow in vivo (36, 37) should require the FN/integrin/PDE4D5/B55α pathway. To test this hypothesis, we compared vessels from chow-fed WT versus *PDE4D*^{mut} mice on the *ApoE*$^{-/-}$ background, which have increased vascular inflammation but minimal plaque formation. The

increased Yap accumulation in ECs in the atherosclerosis-prone inner curvature of the aortic arch from WT mice was significantly blunted in *PDE4D*^{mut} mice (Figure 7A). Furthermore, expression of the Yap target genes Cyr61 and CTGF in the inner curvature was significantly decreased in *PDE4D*^{mut} mice (Figure 7B and Supplemental Figure 7). Together, these data identify Yap as a direct target of the PP2A-B55α complex that is regulated through PDE4D5.

Discussion

These results show, first, that blocking the binding of PDE4D5 to integrin α5 reduced EC inflammatory activation and atherosclerotic plaque burden and increased plaque stability. Together with the previous findings that mutation of the integrin α5 cytoplasmic domain inhibited these events, these data provide conclusive evidence that α5-PDE4D5 interaction contributes to inflammatory activation of the endothelium and to atherosclerosis. The evidence of increased plaque stability is notable in light of the decreased plaque stability after deletion of plasma FN (26). FN therefore appears to promote inflammation and plaque expansion through α5/PDE signaling, whereas the enhancement of plaque stability is separable, probably through the role of FN role in scaffolding collagen fibrillogenesis (42). The PDE4D5 mutation also slightly improved, or at least did not inhibit, vascular remodeling in the hindlimb ischemia model. The integrin/PDE4D5 pathway, unlike FN itself, may therefore be a suitable therapeutic target.

Our investigation of the mechanism of PDE4D5 activation led to the unanticipated finding that FN and PDE4D5 control the assembly of a B55α-containing PP2A complex. This complex localizes to sites of adhesion and dephosphorylates the inhibitory S651 site on PDE4D5. PDE4D5 is therefore both upstream and downstream of PP2A. Given the paucity of phosphatase complexes compared with phosphorylated residues in the proteome, other relevant B55α-PP2A substrates seemed likely. As large-scale phospho-proteomic profiling would not distinguish direct B55α-PP2A substrates from secondary changes, we took a candidate approach. Several reports in the literature suggested the Hippo/Yap pathway as a possible target. Indeed, plating cells on FN induced Yap dephosphorylation on key regulatory sites, indicative of Yap activation. Adherence to FN also blocked disturbed-flow–induced Yap phosphorylation (inhibition), thereby increasing nuclear translocation and Yap-target gene expression and stabilizing Yap protein. The B55α-PP2A complex directly dephosphorylated Yap, as indicated by the lack of effect on the upstream kinase LATS, the co-IP of Yap and PP2A, and the in vitro dephosphorylation with purified components. Consistent with these in vitro results, the reported stabilization of Yap at atherosclerosis-prone regions of arteries (36, 37) was blunted in *PDE4D5*^{mut} mice. As Yap inactivation in ECs potently reduced atherosclerosis in mice (36, 37), this pathway appears to substantially contribute to the effects of the FN/α5/PDE4D5 pathway in vascular disease.

These experiments were conducted using matrix proteins adsorbed at low concentrations to rigid glass or plastic and are thus distinct from the regulation of Yap by matrix stiffness (43, 44). The results, however, fit with the well-known ability of FN to promote EC cell-cycle progression relative to laminin and collagen (45), as well as inflammatory activation (2, 9). Both mechanical and biochemical signaling mechanisms may contribute in vivo, where atherosclerosis and aging are associated with increased matrix stiffness (46). How specific integrin α5 signaling and matrix stiffness interact to regulate Yap activation and gene expression will be interesting to explore in future work.

Binding of cell-derived FN that contains the alternatively spiced EDA domain, but not plasma FN, to TLR4 has been implicated in flow-dependent vascular inflammation and atherosclerosis (16, 47). Supporting this idea, both TLR4 and EDA$^+$ FN are increased in atherosclerotic lesions (48). Interestingly, there is considerable overlap between the effects of EDA deletion in these studies and blockade of PDE4D binding in our work. This could be explained if TLR4 proinflammatory signaling is dampened by cAMP/PKA, such that EDA/TLR4 signaling requires the integrin α5/PDE4D pathway. EDA also promotes FN matrix assembly (49), thus, deletion of the EDA domain may decrease the amount of FN in the vessel wall, thereby influencing all FN-dependent pathways.

The molecular mechanism by which PDE4D5 controls B55α-PP2A assembly is unknown. In vitro Yap dephosphorylation experiments indicate that PDE4D5 is not required for B55α-PP2A assembly in solution, as expected from published data (50). PDE4D5 might block inhibitory factors or protein modifications of B55α to facilitate holoenzyme assembly in vivo. Elucidation of the detailed mechanism is an important question for further analysis.

Atherogenesis shares features with the physiological vascular remodeling that promotes efficient perfusion of tissues via angiogenesis and modulation of vessel diameter (10, 11). These processes involve changes in the extracellular matrix (ECM), inflammatory activation of the endothelium, and recruitment of leukocytes that assist with remodeling, followed by resolution of inflammation and restoration of stable vasculature. EC responses to disturbed flow at artery branches and regions of high curvature may be seen as futile, flow-dependent remodeling that synergizes with systemic inflammatory and metabolic stresses to induce atherogenesis. By contrast, physiological remodeling is suppressed by an elevated inflammatory status and metabolic disorders (51–54). It is well accepted that cAMP/PKA activation is antiinflammatory and reduces plaque burden (55–57). However, cAMP/PKA signaling is highly multifunctional, with distinct effects in the heart, brain, liver, and other tissue and thus is not an attractive target for systemic therapy. Treating vascular disease requires more precise methods to reduce chronic vascular inflammation without harmful side effects. Therapeutic targeting of interactions within the α5/PDE4D5/PP2A pathway, therefore, appears to be a promising approach.

In summary, our data elucidate a pathway in which FN binding to the integrin α5 subunit recruits PDE4D5 to induce assembly of a PP2A-B55α complex that regulates flow-induced Yap signaling and very likely other functionally relevant effectors. This pathway is likely to have widespread implications for the control of cell phenotype by the ECM across a range of systems. Important questions for future work include determining the mechanism by which PDE4D enhances PP2A-B55α association on FN, identifying additional matrix-dependent substrates for PP2A, and elucidating the role of this pathway in controlling the EC phenotype.

Methods

Generation of PDE4D^{mut} *mice. PDE4D*^{mut} mice were generated at the Yale Genome Editing Center. We used the double-nicking strategy to min-

imize off-target effects (24, 58, 59). Two guide RNA sequences were selected from candidate sequences using a Zhang laboratory algorithm (http://crispr.mit.edu/). Guide A: CUUUUCCUUCUGAGUUGGAGAGG; guide B: GGCCGAUGUCGCAGAUCAGUGGG. The donor ssDNA oligonucleotide (ssODN) template including PDE4D mutations was synthesized (IDT; Ultramer grade), and the sequence follows: 5′-ATGAGTCGGTCTGGCAACCAGGTGTCGGAGTACATCTCAAACACATTTCTCGATAAGCAACATGAAGTGGAAATCCCCTCTCCAACGCAGAAGGAAAAAGAGGAGGAGGAAGAGCCGATGTGCAGATCAGTGGGGTCAAGAAGTTGATGCACAGCTCCAGCCCTAACTAATTCATGTATC-3′.

Templates for in vitro transcription of the sgRNAs were PCR amplified from the pX335 plasmid (a gift from Feng Zhang, Addgene plasmid 42335) using the following primers: forward primer for guide A, 5′-TGTAATACGACTCACTATAGGCTTTTCCTTCTGAGTTGGAGGTTTTAGAGCTAGAAATAGC-3′ (T7 promoter/guide/sg scaffold template); forward primer for guide B, 5′-TGTAATACGACTCACTATtAGGGGCCGATGTCGCAGATCAGTGTTTTAGAGCTAGAAATAGC-3′; reverse primer, 5′-AGCACCGACTCGGTGCCACT-3′, reverse primer, 5′-AGCACCGACTCGGTGCCACT-3′.

The DNA template for in vitro transcription of Cas9 mRNA was PCR amplified from pX335, in vitro transcribed, and purified as described previously (58). Cas9 mRNA (100 ng/μL), guide A and guide B sgRNAs (50 ng/μL each), and the ssODN template (100 ng/μL) were microinjected into the cytoplasm of C57Bl/6J zygotes; surviving zygotes were transferred to oviducts of CD-1 pseudopregnant females on the day of injection as described previously (60).

For genotyping, the primers for the WT allele (200-bp PCR product) were forward: 5′-GATACCAACTTGTAGTCAACTC-3′; reverse: 5′-TCGGCCTTTTCTTCTTCTCCTT-3′; and for the mutant allele (200-bp PCR product), the same forward primer as the WT allele was used; reverse: 5′-TCGGCTCTTCCTCCTCCTCTTTT-3′.

Histology and IHC. Mice were euthanized according to the Yale University IACUC protocol and perfused via the left ventricle with PBS and then 3.7 % formaldehyde for fixation. For IHC, longitudinal paraffin-embedded sections of aortae were prepared by the Yale Pathology Tissue Services. For cryosections of aortic roots, fixed tissue was kept in 30% sucrose in PBS at 4°C overnight, incubated with a 1:1 mixture of OCT and 30% sucrose and PBS for 30 minutes, and embedded in OCT on dry ice. Aortic root cryosections (10-μm-thick) were prepared with a cryostat and incubated in blocking buffer containing 5% goat serum, 0.1% Triton X-100, and PBS for 1 hour at room temperature. Sections were incubated in primary Abs at the indicated concentrations in blocking buffer overnight at 4°C, washed 3 times in PBS, and then incubated with Alexa Fluor 568–conjugated secondary Abs (1:300, Invitrogen, Thermo Fisher Scientific) for 1 hour at room temperature. After washing with PBS, sections were mounted in Fluoromount G (Southern Biotech). The following Abs were used: anti-VCAM1 (Abcam, ab955, 1:300); anti-ICAM1 (BioLegend, 116102, 1:400); anti–p–NF-κB (Abcam, ab28856, 1:400); anti-CD68 (Abcam, ab955, 1:400); anti-SMA (MilliporeSigma, C6198, 1:500); anti-MMP2 (Santa Cruz Biotechnology, sc10736, 1:100); and anti-MMP9 (Abcam, ab38898, 1/500). Six mice (3 male and 3 female, 3 months of age) were examined for inflammatory markers in the aortic arch for each strain. For atherosclerosis, 3-month-old homozygous *PDE4D^{mut} ApoE$^{-/-}$* mice were placed on a high-fat diet (Open Source, D12079B) for 4 months, euthanized, and their tissues fixed and examined as described above. For histological analysis, Oil Red O (0.3%, MilliporeSigma) and Picrosirius red stains (Abcam) were used. All stained sections were imaged on a Nikon 80i microscope. Image analysis was done using ImageJ software (NIH). Areas of Oil Red O–stained aortic roots were quantified and expressed as the percentage of the total cross-sectional area of the aortic root. Picrosirius red–positive areas were expressed as a percentage of the plaque area.

Hindlimb ischemia. Femoral arteries were ligated at 2 locations spaced 5-mm apart, and the arterial segment between the ligation was excised. Blood flow in the hind limbs was imaged using a Moor Infrared Laser Doppler Imager (LDI) (Moor Instruments Ltd.) at 37.0°C to 38.0°C under ketamine/xylazine (80:5 mg/kg) anesthesia. Data were analyzed with Moor LDI image processing software, version 3.09, and plotted as the ratio of flow in the right/left (R/L) hind limb.

μCT angiography. 2D μCT scans were performed with a GE eXplore MS Micro-CT System, using a 400 cone beam with an angular increment of 0.5° and 8- to 27-μm slice thickness at a voltage of 163.2 mAs, 80 kVp. Data were transferred to a Dell Dimension computer with 3D volume–rendering software, version 3.1 (Vital Images Inc.) and MicroView software, version 1.15 (GE Medical System). ImageJ and Image-Pro Plus (Media Cybernetics) software programs were used to analyze vessel numbers, diameter, area, and volume, as well as arterial density.

In situ zymography. Unfixed aortic root cryosections were incubated with DQ-gelatin (20 μg/mL) in gelatinase reaction buffer at 37°C for 1 hour, washed with PBS, and mounted with antifade mounting solution.

Cell culture. Primary bovine aortic ECs (BAECs) were purchased from VEC Technologies and grown in DMEM containing 10% FBS and penicillin/streptomycin. HUVECs were purchased from the Yale VBT tissue culture core and grown in M199, 20% FBS, 5 mg/mL ECGS, 100 μg/mL heparin, and penicillin/streptomycin.

Shear stress experiments. Serum-starved ECs were replated on glass slides coated with the indicated proteins for 6 hours before application of flow. The slides were loaded into parallel plate flow chambers. Laminar shear at 15 dynes/cm^2 was used to mimic high flow in atherosclerosis-resistant regions of arteries. OSS of 1 ± 5 dynes/cm^2, 1 Hz, was used to mimic disturbed flow in atherosclerosis-prone regions.

Immunoprecipitation. Cells were lysed in 20 mM PIPES, pH 6.8, 1% Triton X-100, 150 mM NaCl, 150 mM sucrose, 0.2% sodium deoxycholate, 500 μM EDTA, and protease inhibitors. After incubation on ice for 15 minutes, samples were centrifuged at 20,000 *g* for 10 minutes, and supernatants were diluted 10× in buffer containing 20 mM PIPES, pH 6.8, 1% Triton X-100, 150 mM NaCl, 150 mM sucrose, 2.5 mM $MgCl_2$, and 2.5 mM $MnCl_2$. For immunoprecipitation (IP) of GFP-B55α, GFP trap agarose beads (ChromoTek) were incubated with the lysates for 3 hours at 4°C before washing with dilution buffer. For IP of endogenous B55α, a B55α Ab (clone 2G9, MiliporeSigma) was covalently cross-linked with agarose beads using the Pierce Crosslink IP Kit (Thermo Fisher Scientific).

Immunoblotting. The Abs used for Western blotting were as follows: anti–p-NF-κB–p65 (S536), rabbit mAb (93H1) (Cell Signaling Technology, 3033L, 1:1000); anti–NF-κB–p65, mouse mAb (F-6) (Santa Cruz Biotechnology, sc-8008, 1:1000); anti-PP2A, C subunit, mouse mAb (BD Transduction Laboratories, 610556, 1:1000); anti-PP2A, B55α, mouse mAb (2G9) (Cell Signaling Technology, 5689s, 1:1000); anti-PP2A, A subunit, rabbit mAb (81G5) (Cell Signaling Technology, 2041s, 1:1000); anti–p-LATS1(T1079), rabbit mAb (D57D3) (Cell

Signaling Technology, 8654s, 1:1000); anti-LATS1, rabbit polyclonal Ab (pAb) (Abcam, ab70565, 1:1000); anti–p-Yap (S127), rabbit pAb (Cell Signaling Technology, 4911s, 1:1000); anti–p-Yap (S381), rabbit mAb (D1E7Y) (Cell Signaling Technology, 13169s, 1:1000); anti-Yap, mouse mAb (63.7) (Santa Cruz Biotechnology, sc-101199, 1:200); anti–p-eNOS (S635), rabbit pAb (Upstate, 07-562, 1:1000); and anti-eNOS, rabbit pAb (BD, 610298, 1:1000).

Band intensities from immunoblotting were quantified by densitometry with ImageJ software.

Glutathione S-transferase pull-down assays. Glutathione S-transferase (GST) fusion proteins (5 μg) on GSH-agarose beads were incubated with 1.5 μg B55α purified from insect cells in buffer containing 20 mM PIPES, pH 6.8, 1% Triton X-100, 500 mM NaCl, 0.1% sodium deoxycholate, 150 mM sucrose ,and 1 mg/mL BSA for 30 minutes at 4°C, and then washed and analyzed using SDS-PAGE and Western blotting.

Plasmids and siRNA. Human PDE4D5 WT and the PDE4D5-dN mutant were PCR amplified and cloned into the pLVX-mCherry-N1 vector (Clontech) using Gibson assembly after vector digestion with XhoI and EcoRI. WT forward primer, 5′-AGCGCTACCGGACTCAGATCTCGAGATGGCTCAGCAGACAAGCCCGG-3′, dN forward primer, 5′-AGCGCTACCGGACTCAGATCTCGAATGCAAACGACGGGAGTCCTTCCTGTATC-3′; reverse primer, 5′-CGCGGTACCGTCGACTGCAGAATTCGCGTGTCAGGAGAACGATCATCTA-3′. Human B55α was PCR amplified from HUVEC cDNA and cloned into pEGFP-C1 (Clontech) using HindIII and BamHI sites. Forward primer, 5′-GCAAGCTTCGATGTTCCCGAAGTTTTCTCTTCG-3′; reverse primer, 5′-GCGGATCCCTAATTCACTTTGTCTTGAAATAT-3′. GFP-tagged B55α was PCR amplified from pEGFP-C1-B55α and cloned into pLPCX (Clontech) using NotI and ClaI sites. Forward primer, 5′-GCGCGGCCGCATGGTGAGCAAGGGCGAGGA-3′; reverse primer, 5′-GCATCGATCTAATTCACTTTGTCTTGAAATAT. The siRNA sequence for PDE4D used in BAECs and HUVECs was 5′-AAGAACUUGCCUUGAUGUACA-3′ (9). The siRNAs for B55α were no. 1, 5′-GCAGAUGAUUUGCGGAUUAUU-3′ and no. 2, 5′GUGCAAGUGGCAAGCGAAAUU-3′. PDE4D5 fragments cloned into pGEX-4T1 were previously described (61).

Proteomic analysis for PDE4D5 binding proteins. The GFP-tagged PDE4D5-S651E mutant was stably expressed in BAECs using retroviral infection. The cells were detached and kept in suspension for 30 minutes, replated on FN or MG for 20 minutes, and then lysed and immunoprecipitated with GFP-Trap. After SDS-PAGE and silver staining, specific bands were excised and submitted to the Yale Keck Biotechnology Resource Laboratory for LC–tandem MS (LC-MS/MS) analysis.

Statistics. Statistics were analyzed by 2-tailed Student's *t* test or 1-way ANOVA (for multiple comparisons) using GraphPad Prism 6 (GraphPad Software). A *P* value of less than 0.05 was considered statistically significant. Data are presented as the mean ± SEM.

Study approval. Animal experiments were approved by the Yale Institutional Animal Care and Use committee.

Author contributions

SY and MAS designed the project. SY, RH, MES, ANS, and ZZ conducted the experiments and analyzed the data. SY and MAS generated the figures and wrote the manuscript. AJK and DCP provided technical advice and edited the manuscript. MAS directed and supervised the project.

Acknowledgments

We thank Jiasheng Zhang (Yale University) for assistance with mouse femoral artery ligation (FAL) surgery and Stefano Piccolo (University of Padova, Italy) for providing Flag-Yap DNA and for critical comments on the manuscript. Lipid analysis was done by the Yale Mouse Phenotypic Center, which is supported by NIH grant U24 DK059635. This work was funded by NIH grants 5R01HL75092, RO1 HL135582, and PO1107205 (to MAS) and R01s MH115939, NS105640, and NS089662 (to AJK). We are grateful to Rita Webber, Nicole Copeland, and Laran Coon for maintaining the mouse colonies used in this study.

Address correspondence to: Martin A. Schwartz, Yale Cardiovascular Research Center, 300 George St., 7th floor, New Haven, Connecticut 06511, USA. Email: martin.schwartz@yale.edu.

1. Hahn C, Schwartz MA. The role of cellular adaptation to mechanical forces in atherosclerosis. *Arterioscler Thromb Vasc Biol*. 2008;28(12):2101–2107.
2. Yurdagul A, Finney AC, Woolard MD, Orr AW. The arterial microenvironment: the where and why of atherosclerosis. *Biochem J*. 2016;473(10):1281–1295.
3. Grant DS, Kleinman HK, Martin GR. The role of basement membranes in vascular development. *Ann N Y Acad Sci*. 1990;588:61–72.
4. Orr AW, Sanders JM, Bevard M, Coleman E, Sarembock IJ, Schwartz MA. The subendothelial extracellular matrix modulates NF-kappaB activation by flow: a potential role in atherosclerosis. *J Cell Biol*. 2005;169(1):191–202.
5. Kim S, Bell K, Mousa SA, Varner JA. Regulation of angiogenesis in vivo by ligation of integrin alpha5beta1 with the central cell-binding domain of fibronectin. *Am J Pathol*. 2000;156(4):1345–1362.
6. Chiu CH, Chou CW, Takada S, Liu YW. Development and fibronectin signaling requirements of the zebrafish interrenal vessel. *PLoS One*. 2012;7(8):e43040.
7. Yurdagul A, Finney AC, Woolard MD, Orr AW. The arterial microenvironment: the where and why of atherosclerosis. *Biochem J*. 2016;473(10):1281–1295.
8. Funk SD, Yurdagul A, Green JM, Jhaveri KA, Schwartz MA, Orr AW. Matrix-specific protein kinase A signaling regulates p21-activated kinase activation by flow in endothelial cells. *Circ Res*. 2010;106(8):1394–1403.
9. Yun S, et al. Interaction between integrin α5 and PDE4D regulates endothelial inflammatory signalling. *Nat Cell Biol*. 2016;18(10):1043–1053.
10. Baeyens N, Bandyopadhyay C, Coon BG, Yun S, Schwartz MA. Endothelial fluid shear stress sensing in vascular health and disease. *J Clin Invest*. 2016;126(3):821–828.
11. Wragg JW, Durant S, McGettrick HM, Sample KM, Egginton S, Bicknell R. Shear stress regulated gene expression and angiogenesis in vascular endothelium. *Microcirculation*. 2014;21(4):290–300.
12. Feaver RE, Gelfand BD, Wang C, Schwartz MA, Blackman BR. Atheroprone hemodynamics regulate fibronectin deposition to create positive feedback that sustains endothelial inflammation. *Circ Res*. 2010;106(11):1703–1711.
13. Gelfand BD, et al. Hemodynamic activation of beta-catenin and T-cell-specific transcription factor signaling in vascular endothelium regulates fibronectin expression. *Arterioscler Thromb Vasc Biol*. 2011;31(7):1625–1633.
14. Kakolyris S, Karakitsos P, Tzardi M, Agapitos E. Immunohistochemical detection of fibronectin in early and advanced atherosclerosis. *In Vivo*. 1995;9(1):35–40.
15. Tan MH, Sun Z, Opitz SL, Schmidt TE, Peters JH, George EL. Deletion of the alternatively spliced fibronectin EIIIA domain in mice reduces atherosclerosis. *Blood*. 2004;104(1):11–18.
16. Babaev VR, Porro F, Linton MF, Fazio S, Baralle FE, Muro AF. Absence of regulated splicing of fibronectin EDA exon reduces atherosclerosis in mice. *Atherosclerosis*. 2008;197(2):534–540.
17. Rohwedder I, et al. Plasma fibronectin deficiency impedes atherosclerosis progression and fibrous cap formation. *EMBO Mol Med*. 2012;4(7):564–576.
18. Orr AW, Hahn C, Blackman BR, Schwartz MA.

p21-activated kinase signaling regulates oxidant-dependent NF-kappa B activation by flow. *Circ Res*. 2008;103(6):671–679.
19. Yurdagul A, Chen J, Funk SD, Albert P, Kevil CG, Orr AW. Altered nitric oxide production mediates matrix-specific PAK2 and NF-κB activation by flow. *Mol Biol Cell*. 2013;24(3):398–408.
20. Budatha M, et al. Inhibiting integrin α5 cytoplasmic domain signaling reduces atherosclerosis and promotes arteriogenesis. *J Am Heart Assoc*. 2018;7(3):e007501.
21. Al-Yafeai Z, Yurdagul A, Peretik JM, Alfaidi M, Murphy PA, Orr AW. Endothelial FN (fibronectin) deposition by α5β1 integrins drives atherogenic inflammation. *Arterioscler Thromb Vasc Biol*. 2018;38(11):2601–2614.
22. Gupton SL, et al. Mena binds α5 integrin directly and modulates α5β1 function. *J Cell Biol*. 2012;198(4):657–676.
23. Jin SL, Richard FJ, Kuo WP, D'Ercole AJ, Conti M. Impaired growth and fertility of cAMP-specific phosphodiesterase PDE4D-deficient mice. *Proc Natl Acad Sci U S A*. 1999;96(21):11998–12003.
24. Ran FA, et al. Double nicking by RNA-guided CRISPR Cas9 for enhanced genome editing specificity. *Cell*. 2013;154(6):1380–1389.
25. Yun S, et al. Interaction between integrin α5 and PDE4D regulates endothelial inflammatory signalling. *Nat Cell Biol*. 2016;18(10):1043–1053.
26. Rohwedder I, et al. Plasma fibronectin deficiency impedes atherosclerosis progression and fibrous cap formation. *EMBO Mol Med*. 2012;4(7):564–576.
27. Jaipersad AS, Lip GY, Silverman S, Shantsila E. The role of monocytes in angiogenesis and atherosclerosis. *J Am Coll Cardiol*. 2014;63(1):1–11.
28. Chiang HY, Korshunov VA, Serour A, Shi F, Sottile J. Fibronectin is an important regulator of flow-induced vascular remodeling. *Arterioscler Thromb Vasc Biol*. 2009;29(7):1074–1079.
29. Francis SE, et al. Central roles of alpha5beta1 integrin and fibronectin in vascular development in mouse embryos and embryoid bodies. *Arterioscler Thromb Vasc Biol*. 2002;22(6):927–933.
30. Limbourg A, Korff T, Napp LC, Schaper W, Drexler H, Limbourg FP. Evaluation of postnatal arteriogenesis and angiogenesis in a mouse model of hind-limb ischemia. *Nat Protoc*. 2009;4(12):1737–1746.
31. Janssens V, Longin S, Goris J. PP2A holoenzyme assembly: in cauda venenum (the sting is in the tail). *Trends Biochem Sci*. 2008;33(3):113–121.
32. Bousquet E, et al. RhoB loss induces Rac1-dependent mesenchymal cell invasion in lung cells through PP2A inhibition. *Oncogene*. 2016;35(14):1760–1769.
33. Janssens V, Zwaenepoel K, Rossé C, Petit MM, Goris J, Parker PJ. PP2A binds to the LIM domains of lipoma-preferred partner through its PR130/B″ subunit to regulate cell adhesion and migration. *J Cell Sci*. 2016;129(8):1605–1618.
34. Boo YC, et al. Shear stress stimulates phosphorylation of eNOS at Ser(635) by a protein kinase A-dependent mechanism. *Am J Physiol Heart Circ Physiol*. 2002;283(5):H1819–H1828.
35. de Hoog CL, Foster LJ, Mann M. RNA and RNA binding proteins participate in early stages of cell spreading through spreading initiation centers. *Cell*. 2004;117(5):649–662.
36. Wang KC, et al. Flow-dependent YAP/TAZ activities regulate endothelial phenotypes and atherosclerosis. *Proc Natl Acad Sci U S A*. 2016;113(41):11525–11530.
37. Wang L, et al. Integrin-YAP/TAZ-JNK cascade mediates atheroprotective effect of unidirectional shear flow. *Nature*. 2016;540(7634):579–582.
38. Zhao B, et al. Inactivation of YAP oncoprotein by the Hippo pathway is involved in cell contact inhibition and tissue growth control. *Genes Dev*. 2007;21(21):2747–2761.
39. Zhao B, Li L, Tumaneng K, Wang CY, Guan KL. A coordinated phosphorylation by Lats and CK1 regulates YAP stability through SCF(beta-TRCP). *Genes Dev*. 2010;24(1):72–85.
40. Rouleau C, et al. Transformation by polyomavirus middle T antigen involves a unique bimodal interaction with the Hippo effector YAP. *J Virol*. 2016;90(16):7032–7045.
41. Ogris E, et al. A protein phosphatase methylesterase (PME-1) is one of several novel proteins stably associating with two inactive mutants of protein phosphatase 2A. *J Biol Chem*. 1999;274(20):14382–14391.
42. Kadler KE, Hill A, Canty-Laird EG. Collagen fibrillogenesis: fibronectin, integrins, and minor collagens as organizers and nucleators. *Curr Opin Cell Biol*. 2008;20(5):495–501.
43. Halder G, Dupont S, Piccolo S. Transduction of mechanical and cytoskeletal cues by YAP and TAZ. *Nat Rev Mol Cell Biol*. 2012;13(9):591–600.
44. Dupont S. Role of YAP/TAZ in cell-matrix adhesion-mediated signalling and mechanotransduction. *Exp Cell Res*. 2016;343(1):42–53.
45. Wary KK, Mainiero F, Isakoff SJ, Marcantonio EE, Giancotti FG. The adaptor protein Shc couples a class of integrins to the control of cell cycle progression. *Cell*. 1996;87(4):733–743.
46. VanderBurgh JA, Reinhart-King CA. The role of age-related intimal remodeling and stiffening in atherosclerosis. *Adv Pharmacol*. 2018;81:365–391.
47. Qu D, et al. Focal TLR4 activation mediates disturbed flow-induced endothelial inflammation [published online ahead of print February 20, 2019]. *Cardiovasc Res*. https://doi.org/10.1093/cvr/cvz046.
48. Edfeldt K, Swedenborg J, Hansson GK, Yan ZQ. Expression of toll-like receptors in human atherosclerotic lesions: a possible pathway for plaque activation. *Circulation*. 2002;105(10):1158–1161.
49. Guan JL, Trevithick JE, Hynes RO. Retroviral expression of alternatively spliced forms of rat fibronectin. *J Cell Biol*. 1990;110(3):833–847.
50. Xu Y, Chen Y, Zhang P, Jeffrey PD, Shi Y. Structure of a protein phosphatase 2A holoenzyme: insights into B55-mediated Tau dephosphorylation. *Mol Cell*. 2008;31(6):873–885.
51. Jang JJ, Ho HK, Kwan HH, Fajardo LF, Cooke JP. Angiogenesis is impaired by hypercholesterolemia: role of asymmetric dimethylarginine. *Circulation*. 2000;102(12):1414–1419.
52. Ali M, et al. Essential role of IL-12 in angiogenesis in type 2 diabetes. *Am J Pathol*. 2017;187(11):2590–2601.
53. Dunn LL, et al. A critical role for thioredoxin-interacting protein in diabetes-related impairment of angiogenesis. *Diabetes*. 2014;63(2):675–687.
54. van Weel V, et al. Hypercholesterolemia reduces collateral artery growth more dominantly than hyperglycemia or insulin resistance in mice. *Arterioscler Thromb Vasc Biol*. 2006;26(6):1383–1390.
55. Ouchi N, et al. Adiponectin, an adipocyte-derived plasma protein, inhibits endothelial NF-kappaB signaling through a cAMP-dependent pathway. *Circulation*. 2000;102(11):1296–1301.
56. Lee JH, et al. Cilostazol reduces atherosclerosis by inhibition of superoxide and tumor necrosis factor-alpha formation in low-density lipoprotein receptor-null mice fed high cholesterol. *J Pharmacol Exp Ther*. 2005;313(2):502–509.
57. Indolfi C, et al. Activation of cAMP-PKA signaling in vivo inhibits smooth muscle cell proliferation induced by vascular injury. *Nat Med*. 1997;3(7):775–779.
58. Yang H, Wang H, Jaenisch R. Generating genetically modified mice using CRISPR/Cas-mediated genome engineering. *Nat Protoc*. 2014;9(8):1956–1968.
59. Wang H, et al. One-step generation of mice carrying mutations in multiple genes by CRISPR/Cas-mediated genome engineering. *Cell*. 2013;153(4):910–918.
60. Behringer R. *Manipulating the Mouse Embryo: a Laboratory Manual*. New York, NY: Cold Spring Harbor Laboratory Press; 2014.
61. Kim HW, et al. Cyclic AMP controls mTOR through regulation of the dynamic interaction between Rheb and phosphodiesterase 4D. *Mol Cell Biol*. 2010;30(22):5406–5420.